

Origin of Spinel Nanocheckerboards via First Principles

Mordechai Kornbluth and Chris A. Marianetti*

Department of Applied Physics and Applied Mathematics, Columbia University, New York, New York 10027, USA

(Received 15 January 2015; published 3 June 2015)

Self-organizing nanocheckerboards have been experimentally fabricated in Mn-based spinels but have not yet been explained with first principles. Using density-functional theory, we explain the phase diagram of the $\text{ZnMn}_x\text{Ga}_{2-x}\text{O}_4$ system and the origin of nanocheckerboards. We predict total phase separation at zero temperature and then show the combination of kinetics, thermodynamics, and Jahn-Teller physics that generates the system's observed behavior. We find that the $\{011\}$ surfaces are strongly preferred energetically, which mandates checkerboard ordering by purely geometrical considerations.

DOI: 10.1103/PhysRevLett.114.226102

PACS numbers: 68.65.-k, 61.46.Km, 62.23.St

Experimental observation demonstrates intriguing nanoscale compositional ordering in a variety of material alloys. These include noble-metal-alloy nanocheckerboards [1–3], $\text{BaTiO}_3\text{-CoFe}_2\text{O}_4$ nanopillars [4], and an assortment of manganese-spinel nanocheckerboards [5–9]. Nanoscale phenomena are inherently difficult to treat with quantum mechanics' first principles, due to the prohibitive scaling of electronic-structure methods. Previous theoretical studies [10–14] used phase-field models [15,16] to simulate nanocheckerboard formation. However, those models rely upon coefficients chosen without first-principles justification. In contrast, our work reveals the origin of nanocheckerboards from first principles.

Here we examine the experimentally well-characterized manganite spinels $A^{2+}\text{Mn}_2^{3+}\text{O}_4^{2-}$. These cooperative-Jahn-Teller crystals, upon doping with certain non-Jahn-Teller ions, organize into nanocheckerboards. Experiments showed that high-temperature mixing, followed by slow cooling, yields a spontaneously formed checkerboard whose squares alternate tetragonal Mn-rich and cubic Mn-poor phases. These checkerboards emerge from the cross section of spontaneously aligned nanorods. Yeo *et al.* [5] fabricated self-assembling nanocheckerboards from ZnGa_2O_4 (ZGO) + ZnMn_2O_4 (ZMO), comprised of $\sim 4 \times 4 \times 70 \text{ nm}^3$ nanorods. Later work grew checkerboards with nanorods over 700 nm long on a MgO substrate [6,7]. Checkerboards were later extended to other Mn-based spinels, first $\text{MgMn}_x\text{Fe}_{2-x}\text{O}_4$ [8] and then the tunable-sized checkerboards of $\text{Co}_{0.6}\text{Mn}_x\text{Fe}_{2.4-x}\text{O}_4$ [9]. The latter are notable for a patterning that alternates ferro- and paramagnetic phases, which yields potential for ultra-high-density information storage.

We analyze the nanocheckerboard system $\text{ZnMn}_x\text{Ga}_{2-x}\text{O}_4$, whose relative simplicity renders it a minimal prototype. We sketch the main experimental results of Ref. [5] in Fig. 1. ZGO is a cubic spinel, while ZMO is a tetragonal spinel ($c/a = 1.14$ [17]), which immediately leads to some anomalous differences between the experimental data and naive expectations.

First, room-temperature experiments reveal solid solutions at non-negligible concentrations, despite the disparate crystal structures of the end members, in violation of the Hume-Rothery rules. Second, x-ray diffraction experiments show a cubic structure up to 25% ZMO (and 75% ZGO), whereas a non-negligible tetragonality would be expected at this concentration, regardless of the origin of the observed solubility. Third, in the region where ZMGO phase separates, the experimental data show checkerboard formations instead of traditional spinodal decomposition.

To address these issues, we compute the energetics of $\text{ZnMn}_x\text{Ga}_{2-x}\text{O}_4$ using density-functional theory (DFT) as implemented in the Vienna *ab initio* simulation package (VASP) [18–21]. We use a plane-wave cutoff energy of 415 eV, the PW91 generalized gradient approximation (GGA) functional [22,23], and projector augmented wave based pseudopotentials [24]. All calculations are initialized with ferromagnetic ordering for simplicity, a well-justified approach for the Néel temperature of merely $\approx 20 \text{ K}$ [17,25,26]. We compute a phase diagram via a cluster expansion [27] of the DFT energetics with Monte Carlo simulations, as implemented in the Alloy Theoretic Automated Toolkit (ATAT) package [28–31].

Both ZGO and ZMO crystallize in the spinel structure, with nominal valences of $\text{Zn}^{2+}(\text{Ga, Mn})_2^{3+}\text{O}_4^{2-}$. Zn occupies the tetrahedral (“A”) sites and Ga/Mn occupy the octahedral (“B”) sites, with negligible inversion [32,33]. Therefore, our study focuses on the effect of Ga/Mn occupation of the B sites. Each B-centered octahedron shares edges with six others, which couples their anionic distortions. ZGO forms a cubic spinel (space group $Fd\bar{3}m$) [33], while ZMO is a tetragonal spinel (space group $I4_1/amd$) with significant distortion $c/a = 1.14$ [17]. The T' of Fig. 1 (high-temperature fully mixed ZMGO) has $c/a \approx 1.06$ [5]. We have provided lattice constants from the literature, and their DFT-calculated analogs, in Supplemental Material (Table S1) [34]; DFT calculations agree with experiment. ZMO's sizable tetragonal distortion is due to the Jahn-Teller (JT) effect in the Mn^{3+} ions, where

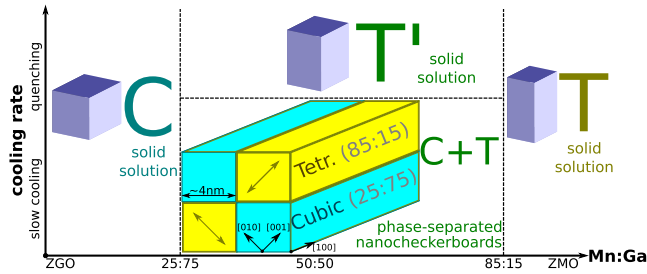


FIG. 1 (color online). Sketch of experimental results presented in Ref. [5]. For $x_{\text{Mn}} \leq 0.25$ a single-phase cubic structure (C) appears, while for $x_{\text{Mn}} \geq 0.85$ it is a single-phase tetragonal structure (T). For intermediate concentrations, a single-phase tetragonal structure (T') is observed upon rapid quenching (the high-temperature phase), while slower cooling generates phase-separated nanocheckerboards with (011) and (01 $\bar{1}$) interfaces. Arrows in the tetragonal regions show the tetragonally elongated direction. The concentrations on the abscissa are those for which data were reported in Ref. [5]. The concentrations within the nanocheckerboards were not reported as being measured directly.

the d^4 configuration in a high-spin octahedral environment causes the e_g orbitals to break symmetry by a tetragonal distortion. This orbital ordering leads to a martensitic cubic-to-tetragonal transition in a variety of crystals, including spinels [39–43]. For consistency, we take [001] to be the JT-distorted direction.

Experiments, summarized in Fig. 1, show solid solutions for $x_{\text{Mn}} \leq 0.25$ and $x_{\text{Mn}} \geq 0.85$. Yet the cubic and strongly tetragonal crystal structures of the end members are expected to be immiscible: Placing a non-JT octahedron in a tetragonal JT-active environment, and vice versa, costs energy. Our DFT calculations quantitatively verify the qualitative Hume-Rothery rules: We generated 192 supercells (≤ 42 atoms) and then fully relaxed the structures. (See Supplemental Material [34] for further calculation details.) Figure 2(a) shows their formation energies, demonstrating that mixing the disparate crystal structures incurs an energy cost [44]. A ground-state search using the cluster expansion (via the aforementioned ATAT package) revealed no lower-energy supercells. Therefore, the zero-temperature ground state of ZMGO is actually phase separation into bulk ZGO and ZMO, a conclusion absent from previous non-first-principles analyses [11–14]. There is no chemical or physical reason to believe that ZGO and ZMO should mix at anything but elevated temperatures.

To further verify this, we computed a phase diagram via a cluster expansion (CE), using the aforementioned ATAT package. (See Supplemental Material [34] for extensive calculation details, as well as the effect of CE shortcomings.) As shown in Fig. 2(b), the zero-temperature stable phases are immiscible bulk ZGO and ZMO. In fact, the observed miscibility at $x_{\text{Mn}} \leq 0.25$ and $x_{\text{Mn}} \geq 0.85$ is unreasonable at all but extreme temperatures.

We therefore attribute the anomalous miscibility to kinetic limitations, i.e., diffusion constraints. This is

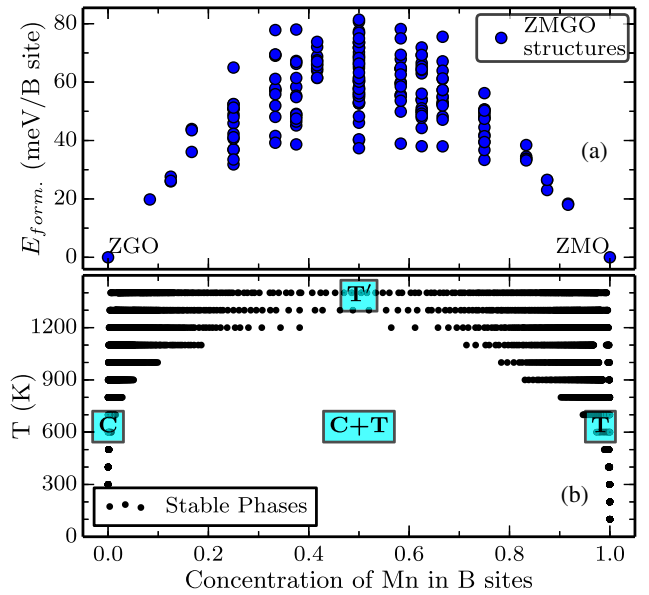


FIG. 2 (color online). (a) Energies of formation of 192 $\text{ZnMn}_x\text{Ga}_{2-x}\text{O}_4$ supercells. (b) Phase diagram of mixed ZGO and ZMO, using ATAT’s EMC2 code. The stable phases (with respect to a semi-grand-canonical ensemble, where x_{Mn} may vary) are shown at varying temperatures. The phases are marked: cubic (C), tetragonal (T), phase-separated (C + T), and high-temperature fully mixed tetragonal (T').

corroborated by the experimental observation that slower cooling (i.e., better diffusion) leads to larger checkers (i.e., less miscibility) [8,9]. In fact, kinetics are the obvious origin of the miscible T' state observed upon rapid quenching (shown in Fig. 1). DFT’s prediction for the T' state for $x_{\text{Mn}} = 0.5$ (taken as the mean of all calculated structures) agrees well with the experimental measurements. For example, DFT predicts $c/a = 1.07$, comparable with the experimental value of $c/a \approx 1.06$. (See Supplemental Material [34] for all data.) Similarly, kinetic limitations must cause the apparent solubility of $x_{\text{Mn}} \leq 0.25$ and $x_{\text{Mn}} \geq 0.85$. For example, if diffusion essentially freezes by, e.g., 900 K, the system cannot separate into 100/0% Mn mixtures and will remain a high-entropy frozen solid solution. Unfortunately, quantitatively predicting kinetics (including checker size) requires detailed knowledge of the diffusion mechanisms, coupled with complex JT lattice dynamics, which is beyond the scope of this Letter.

Having explained that the apparent solubility is due to kinetics, we must address the second anomaly, the experimental observation of a cubic structure for $x_{\text{Mn}} \leq 0.25$. In contrast, DFT predicts a tetragonal structure ($c/a \approx 1.03$ for all calculated structures at $x_{\text{Mn}} = 0.25$) due to the cooperative Jahn-Teller effect.

We propose that the cubic structure of the Mn-poor phase is caused by noncooperative JT distortions at finite temperatures. It is well known that, as in many spinels, ZMO undergoes a phase transition to a cubic spinel above approximately 1323 K, due to noncooperative JT

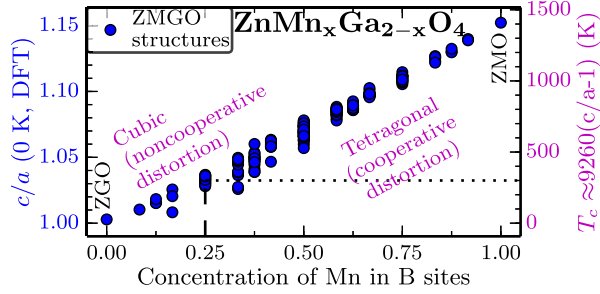


FIG. 3 (color online). Phase diagram for the noncooperative Jahn-Teller transition in spinels. DFT calculates the distortion (left axis) of our ZMGO structures [as in Fig. 2(a)] at 0 K. The critical temperature for the tetragonal-to-cubic transition (right axis) is obtained based on the fitting $T_c \approx 9260(c/a - 1)$ K, empirically accurate for a variety of spinels [40]. Therefore, at room temperature, $x_{\text{Mn}} \lesssim 0.25$ is cubic.

distortions (each octahedron distorting in a random direction) [32,39,40]. The transition temperature scales with doping: Within mean-field theory, it is approximately linear with doping [45]; experimentally, a variety of spinels transition at $T_c \approx 9260(c/a - 1)$ K [40], where c/a is the tetragonal distortion induced by the cooperative distortion [46]. As illustrated in Fig. 3, both these trends imply that, at room temperature, structures of $x \lesssim 0.25$ are cubic due to this transition, while $x \gtrsim 0.25$ are tetragonal. Similar “critical concentrations” of JT ions have been documented in the literature [45,47]. This is also consistent with the conclusion of Noh *et al.* [48] that, although $x_{\text{Mn}} = 0.25$ has an XRD pattern of a cubic spinel, it has a rather large JT splitting of ~ 0.7 eV, i.e., a high-spin electronic configuration, which leads to JT distortion. (See Supplemental Material [34] for detailed analysis of the reliability of GGA’s high-spin prediction.) Therefore, low-temperature measurements should reveal DFT’s tetragonally distorted structure for $x \leq 0.25$.

Therefore, the cubic structure is due to the high-entropy noncooperative distortion. We should note that these finite-temperature Jahn-Teller lattice dynamics are expected to enhance miscibility, as noted by other experiments [49]. For example, whereas the experiment places the boundaries at 25%/85% Mn, our phase diagram [Fig. 2(b)] shows that ZMO is more tolerant of Ga doping than ZGO of Mn doping. This discrepancy is likely due to the lack of noncooperative distortions in the cluster-expansion model, although a quantitative treatment is beyond the scope of this Letter. However, this alone would not suffice to cause appreciable solubility near room temperature.

Now we turn to $0.25 < x_{\text{Mn}} < 0.85$, where slowly cooled samples phase separate on a diffusion-limited scale. We seek to explain how this leads to nanocheckerboards rather than traditional spinodal decomposition. We calculate the energy of joining a slab of ZGO to a slab of ZMO along a particular surface; lower energies indicate preferred interface directions [50]. Figure 4(a) shows the energies of

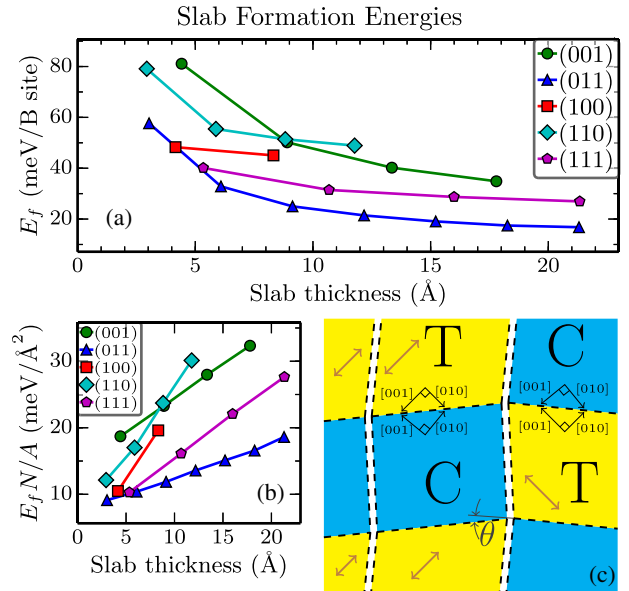


FIG. 4 (color online). (a) Formation energies of ZGO/ZMO slabs layered in the given direction, normalized per B site, plotted against the average thickness t of the ZGO and ZMO slabs. The $t \rightarrow \infty$ limit corresponds to the contribution of B sites far from the interface; finitely valued t averages the contribution of all sites, including those near the interface. See also Figs. 5(b) and 5(c). (b) The same, multiplied by the number of B sites (N) and divided by the interface area (A), giving a per-area normalization. (c) Fitting cubic (C) and tetragonal (T) domains with a coherent interface along $\{011\}$ surfaces. Arrows show the tetragonally elongated direction in corresponding domains. Geometrically, coherent $\{011\}$ C - T interfaces require a slight angular rotation (shown) between adjacent C and T regions. The consequent zigzag interface can match either an extended equivalent domain (illustrated on the left of the subfigure) or a commensurate domain (on the right), forming a checkerboard structure. This generates tetragonal domains rotated by 90° and cubic domains rotated by θ (see the text).

formation for various slab thicknesses. (Larger thicknesses are inaccessible due to large, convergence-challenged supercells.) In agreement with experiment, DFT prefers the $\{011\}$ surfaces. The energy relative to the next-preferred surface is about 10 meV/B (160 meV per cubic unit cell) at only 1.5 nm and presumably larger for the 4 nm nanocheckerboards.

Because of symmetry, only five directions are calculated directly. We search formation energies of multilayer slabs of thickness t oriented in an arbitrary direction \vec{k} by performing an expansion in the symmetry-adapted (tetragonal) harmonics, a standard group-theory methodology [51,52]. It is apparent from Fig. 4(b) that the total formation energy can be approximated by $E(\vec{k}, t) = A[c_a(\vec{k}) + tc_v(\vec{k})]$, where A is the cross-sectional area and c_a and c_v are constants. We perform an expansion of c_a and c_v in the four lowest-order harmonics via a least-squares fit for the five calculated values of \vec{k} . (Fitting data appear in

Supplemental Material [34].) We thus confirm that (011), and equivalently (01 $\bar{1}$), are the lowest-energy surfaces.

Hence, physics dictates that, when our system coherently mixes cubic and tetragonal phases, it forms (011) and (01 $\bar{1}$) interfaces. Now pure geometry dictates checkerboard configurations for coherent interfaces. As shown in Fig. 4(c), due to bent angles at the interfaces, the only configuration that retains a coherent lattice is the checkerboard formation. Experiments observed that alternating cubic phases are rotated by a few degrees, while alternating tetragonal phases are rotated by 90° [5,6,9]. The origin of these measurements appears clearly in Fig. 4(c), with the cubic-phase angle of rotation $\theta_c = \pi/2 - 2\tan^{-1}a/c$. This agrees with measured values within $< 1^\circ$ (see data in Supplemental Material, Table S2 [34]). In this, our checkerboards are directly related to the CoPt cubic-tetragonal nanostructures [1,10] and other lattice-induced interface rotations [53].

Whence does the {011} preference originate? Previous work showed the importance of both strain and local ionic distortions (i.e., $\vec{k} = 0$ phonons) to the Jahn-Teller effect [54]. Our slabs' formation energy consists of strain energy, due to biaxial lattice matching, and contact energy, due to local ionic distortions and local binding energies. Specifically, for two slabs of thickness t joined in direction $\hat{\mathbf{k}}$, we write

$$E_{\text{formation}} = NE_{\text{strain}}(\hat{\mathbf{k}}, t) + AE_{\text{contact}}(\hat{\mathbf{k}}, t), \quad (1)$$

where the units now ensure that the latter two E terms converge for $t \rightarrow \infty$. As shown in Fig. 5(a), the strain energy can be computed directly by relaxing ionic coordinates for ZGO and ZMO separately, with strained lattice vectors (the “strained bulk” calculation). Then the contact energy is simply the difference between the formation energy and the strain energy. (Detailed equations appear in Supplemental Material [34].)

These energies are shown in Figs. 5(b) and 5(c). We note that {111} and especially {011} have negative contact energies, meaning the layered-slab heterostructure is more stable than the strained ZGO and ZMO separated bulk. Hence, the local ionic distortions couple beneficially to the lattice strain; i.e., atomic rearrangements partially alleviate the energy penalties of lattice strain. This is predominantly concentrated in the breathing and tetragonal-distortion local modes (q_1 and q_3 in the notation of Ref. [55]). Remarkably, the contact energy does not converge in the accessible thicknesses, due to the long range of the Jahn-Teller effect. Rather, even a remarkable distance from the surface, interoctahedron coupling leads to intracellular atomic displacement. Therefore, the {011} preference originates in a beneficial coupling between strain and long-range atomic displacements (contrary to previous non-first-principles work neglecting the latter [10–14]).

In conclusion, we have presented the physics of nano-checkerboards based on first-principles calculations. We

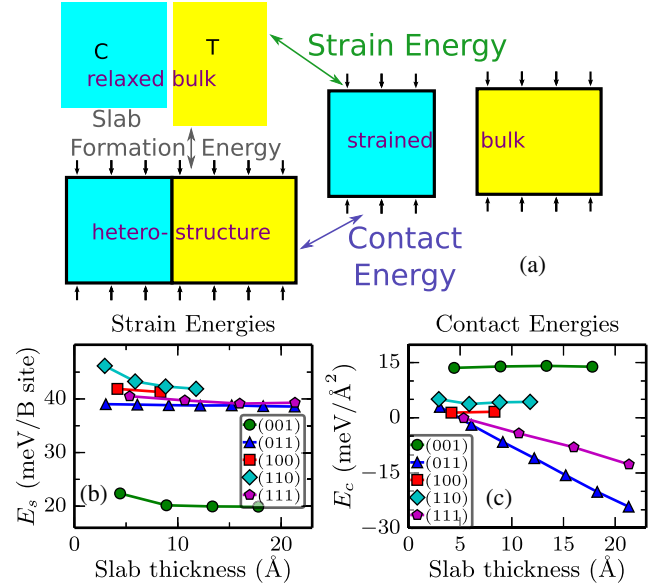


FIG. 5 (color online). (a) Three types of ZMGO structures used to decompose slab formation energies. Black arrows represent cross-sectional biaxial strain, calculated by fully relaxing the heterostructure. All calculations use periodic boundary conditions. (b), (c) Slab formation-energy decomposition, as defined in the text. Motivation for unit choice is described in the text; for comparison, note that a cubic unit cell has 16 B sites and a (100)-cross-sectional area of approximately 74 Å². Negative contact energy, as in the {011} surface, indicates energetic preference for the layered-slab heterostructure over the strained bulk.

established that the thermodynamic ground state is complete phase separation. The incomplete separation originates in diffusion limitations, leading to nanoscale phase domains. We explained the observed cubic crystal structure at $x_{\text{Mn}} = 0.25$ based on noncooperative Jahn-Teller distortions at room temperature. Therefore, although ZMGO's ground state is bulk incoherent, the diffusion-limited structure is bulk coherent (using the terminology of Ref. [56]). This kinetically driven bulk coherence leads to phase separation of cubic and tetragonal phases along {011} surfaces, which we showed from first principles. This, in the presence of kinetic constraints, automatically leads to checkerboards, based on pure geometry. The preference for {011} surfaces originates in beneficial coupling between local distortions and lattice strain. Further quantitative understanding will require robust models for the Jahn-Teller effect in doped materials at finite temperatures.

This research used resources of the National Energy Research Scientific Computing Center, a DOE Office of Science User Facility supported by the Office of Science of the U.S. Department of Energy under Contract No. DE-AC02-05CH11231. The authors acknowledge support from a DARPA Young Faculty Award, Grant No. D13AP00051.

- *chris.marianetti@columbia.edu
- [1] C. Leroux, A. Loiseau, D. Broddin, and G. Vantendelo, *Philos. Mag. B* **64**, 57 (1991).
- [2] K.-I. Udoh, A. M. E. Araby, Y. Tanaka, K. Hisatsune, K. Yasuda, G. V. Tendeloo, and J. V. Landuyt, *Mater. Sci. Eng. A* **203**, 154 (1995).
- [3] H. Winn, Y. Tanaka, T. Shiraishi, K. Udoh, E. Miura, R. I. Hernandez, Y. Takuma, and K. Hisatsune, *J. Alloys Compd.* **306**, 262 (2000).
- [4] H. Zheng, J. Wang, S. E. Lofland, Z. Ma, L. Mohaddes-Ardabili, T. Zhao, L. Salamanca-Riba, S. R. Shinde, S. B. Ogale, F. Bai, D. Viehland, Y. Jia, D. G. Schlom, M. Wuttig, A. Roytburd, and R. Ramesh, *Science* **303**, 661 (2004).
- [5] S. Yeo, Y. Horibe, S. Mori, C. M. Tseng, C. H. Chen, A. G. Khachatryan, C. L. Zhang, and S.-W. Cheong, *Appl. Phys. Lett.* **89**, 233120 (2006).
- [6] S. Park *et al.*, *Nano Lett.* **8**, 720 (2008).
- [7] S. M. O'Malley, P. L. Bonanno, K. H. Ahn, A. A. Sirenko, A. Kazimirov, M. Tanimura, T. Asada, S. Park, Y. Horibe, and S. W. Cheong, *Phys. Rev. B* **78**, 165424 (2008).
- [8] C. L. Zhang, S. Yeo, Y. Horibe, Y. J. Choi, S. Guha, M. Croft, S.-W. Cheong, and S. Mori, *Appl. Phys. Lett.* **90**, 133123 (2007).
- [9] C. L. Zhang, C. M. Tseng, C. H. Chen, S. Yeo, Y. J. Choi, and S. W. Cheong, *Appl. Phys. Lett.* **91**, 233110 (2007).
- [10] Y. Le Bouar, A. Loiseau, and A. G. Khachatryan, *Acta Mater.* **46**, 2777 (1998).
- [11] Y. Ni, Y. M. Jin, and A. G. Khachatryan, *Acta Mater.* **55**, 4903 (2007).
- [12] Y. Ni and A. G. Khachatryan, *Acta Mater.* **56**, 4498 (2008).
- [13] Y. Ni, W. Rao, and A. G. Khachatryan, *Nano Lett.* **9**, 3275 (2009).
- [14] Y. Ni and A. G. Khachatryan, *Nat. Mater.* **8**, 410 (2009).
- [15] W. J. Boettinger, J. A. Warren, C. Beckermann, and A. Karma, *Annu. Rev. Mater. Res.* **32**, 163 (2002).
- [16] I. Steinbach, *Model. Simul. Mater. Sci. Eng.* **17**, 073001 (2009).
- [17] S. Åsbrink, A. Wałkowska, L. Gerward, J. S. Olsen, and E. Talik, *Phys. Rev. B* **60**, 12651 (1999).
- [18] G. Kresse and J. Hafner, *Phys. Rev. B* **47**, 558 (1993).
- [19] G. Kresse and J. Hafner, *Phys. Rev. B* **49**, 14251 (1994).
- [20] G. Kresse and J. Furthmüller, *Comput. Mater. Sci.* **6**, 15 (1996).
- [21] G. Kresse and J. Furthmüller, *Phys. Rev. B* **54**, 11169 (1996).
- [22] J. P. Perdew, J. A. Chevary, S. H. Vosko, K. A. Jackson, M. R. Pederson, D. J. Singh, and C. Fiolhais, *Phys. Rev. B* **46**, 6671 (1992).
- [23] J. P. Perdew, J. A. Chevary, S. H. Vosko, K. A. Jackson, M. R. Pederson, D. J. Singh, and C. Fiolhais, *Phys. Rev. B* **48**, 4978 (1993).
- [24] G. Kresse and D. Joubert, *Phys. Rev. B* **59**, 1758 (1999).
- [25] H. C. Choi, J. H. Shim, and B. I. Min, *Phys. Rev. B* **74**, 172103 (2006).
- [26] H. Li, B. Song, W. J. Wang, and X. L. Chen, *Mater. Chem. Phys.* **130**, 39 (2011).
- [27] A. V. Ruban and I. A. Abrikosov, *Rep. Prog. Phys.* **71**, 046501 (2008).
- [28] A. van de Walle, M. Asta, and G. Ceder, *CALPHAD: Comput. Coupling Phase Diagrams Thermochem.* **26**, 539 (2002).
- [29] A. van de Walle and G. Ceder, *J. Phase Equilib.* **23**, 348 (2002).
- [30] A. Van de Walle and M. Asta, *Model. Simul. Mater. Sci. Eng.* **10**, 521 (2002).
- [31] A. van de Walle, *JOM* **65**, 1523 (2013).
- [32] S. Guillemet-Fritsch, C. Chanel, J. Sarrias, S. Bayonne, A. Rousset, X. Alcobe, and M. L. M. Sarrin, *Solid State Ionics* **128**, 233 (2000).
- [33] D. Errandonea, R. S. Kumar, F. J. Manjón, V. V. Ursaki, and E. V. Rusu, *Phys. Rev. B* **79**, 024103 (2009).
- [34] See Supplemental Material at <http://link.aps.org/supplemental/10.1103/PhysRevLett.114.226102>, which includes Refs. [35–38], for further calculation details, tabulation of extra data, and analysis of Mn's high-spin prediction.
- [35] L. Holliger and R. Besson, *Phys. Rev. B* **83**, 174202 (2011).
- [36] L. J. Nelson, G. L. W. Hart, F. Zhou, and V. Ozoliņš, *Phys. Rev. B* **87**, 035125 (2013).
- [37] L. J. Nelson, V. Ozoliņš, C. S. Reese, F. Zhou, and G. L. W. Hart, *Phys. Rev. B* **88**, 155105 (2013).
- [38] T. Yamanaka, A. Uchida, and Y. Nakamoto, *Am. Mineral.* **93**, 1874 (2008).
- [39] J. Kanamori, *J. Appl. Phys.* **31**, S14 (1960).
- [40] K. S. Irani, A. P. B. Sinha, and A. B. Biswas, *J. Phys. Chem. Solids* **23**, 711 (1962).
- [41] R. Englman, *The Jahn-Teller Effect in Molecules and Crystals* (Wiley-Interscience, New York, 1972).
- [42] G. A. Gehring and K. A. Gehring, *Rep. Prog. Phys.* **38**, 1 (1975).
- [43] K. I. Kugel and D. I. Khomskii, *Sov. Phys. Usp.* **25**, 231 (1982).
- [44] We would rather not blunt Occam's razor and trample intuition by suggesting a long-range-only phase-mixing effect with absolutely no evidence.
- [45] P. Wojtowicz, *Phys. Rev.* **116**, 32 (1959).
- [46] Although our calculations show zero-temperature distortion, while the empirical fitting is for room-temperature distortion, the same experiments [40] show little change in distortion below the transition temperature (< 1%), so the equation is still valid.
- [47] R. Englman and B. Halperin, *Phys. Rev. B* **2**, 75 (1970).
- [48] H.-J. Noh, S. Yeo, J. S. Kang, C. L. Zhang, S. W. Cheong, S. J. Oh, and P. D. Johnson, *Appl. Phys. Lett.* **88**, 081911 (2006).
- [49] S. Yeo, S. Guha, and S. W. Cheong, *J. Phys. Condens. Matter* **21**, 125402 (2009).
- [50] J. Z. Liu, G. Trimarchi, and A. Zunger, *Phys. Rev. Lett.* **99**, 145501 (2007).
- [51] D. B. Laks, L. G. Ferreira, S. Froyen, and A. Zunger, *Phys. Rev. B* **46**, 12587 (1992).
- [52] A. van de Walle, Q. Hong, L. Miljacic, C. B. Gopal, S. Demers, G. Pomrehn, A. Kowalski, and P. Tiwary, *Phys. Rev. B* **89**, 184101 (2014).
- [53] M. Honig, J. A. Sulpizio, J. Drori, A. Joshua, E. Zeldov, and S. Ilani, *Nat. Mater.* **12**, 1112 (2013).
- [54] C. A. Marianetti, D. Morgan, and G. Ceder, *Phys. Rev. B* **63**, 224304 (2001).
- [55] J. H. V. Vleck, *J. Chem. Phys.* **7**, 72 (1939).
- [56] J. Z. Liu and A. Zunger, *Phys. Rev. B* **77**, 205201 (2008).